Journal of Hydrology 619 (2023) 129206

Contents lists available at ScienceDirect

Journal of Hydrology

journal homepage: www.elsevier.com/locate/jhydrol

Research papers

Teleconnection of ENSO extreme events and precipitation variability over the United States

Jai Hong Lee [a,*], Pierre Y. Julien [b], Seungho Lee [c]

[a] Department of Engineering, South Carolina State University, Orangeburg, SC, USA
[b] Department of Civil-Environmental Engineering, Colorado State University, Fort Collins, USA
[c] South Carolina Lexington H. School, Lexington, SC, USA

ARTICLE INFO

This manuscript was handled by A. Bardossy, Editor-in-Chief

Keywords:
Precipitation
Teleconnection
Southern Oscillation
ENSO

ABSTRACT

This study describes a comprehensive investigation of the contiguous United States precipitation patterns in relation to the warm and cold phases of El Niño/southern Oscillation (ENSO) using a set of empirical and statistical analyses, such as harmonic analysis, annual cycle composites, and cross-correlation analysis. Monthly precipitation composites for the first harmonic, covering 24-month ENSO events, are formed for all climate divisions over the United States spanning up to 29 ENSO episodes. From the harmonic vectorial maps plotted on the study area, each vector reveals both intensity and temporal phase of the ENSO-related precipitation teleconnection, and the corresponding candidate and core regions are determined using a machine learning technique of Gaussian Mixture Model (GMM) based on magnitude and temporal phase of climate signal, and Köppen climate classification. As a result of vectorial mapping, five core regions were designated as North-West region (NW), South-West region (SW), Middle-Inland region (MI), South-East region (SE), and North-East region (NE). During fall (0) to spring (+) seasons, the results of this analysis show below (above) normal precipitation response to the El Niño events at the NW region (SW, MI, SE, and NE regions), while the opposite patterns are detected for the cold phase of ENSO. The temporal consistency values were 0.72 to 0.86 (0.77 to 0.82), and spatial coherence values ranged from 0.96 to 0.99 (0.94 to 0.99) for the warm (cold) events. Comparative analyses of precipitation responses to both El Niño and La Niña events reveal the high significance level of the ENSO-related precipitation signals with an opposite tendency in monthly precipitation anomalies. Positive precipitation anomalies during the El Niño thermal forcing are more significant than negative precipitation departures during the La Niña events. Consequently, middle latitude precipitation responses to the El Niño/La Niña phenomena are detectable over the contiguous United States.

1. Introduction

The El Niño/Southern Oscillation (ENSO) is a combined phenomenon of fluctuating sea surface temperature and atmospheric circulation over the central and eastern Pacific Ocean. It has a critical influence on climate patterns all over the world (WMO, 2014). These large-scale naturally occurring phenomena have been investigated at regional and global scale since the extreme phases of the ENSO episodes can cause major hydrologic extremes, e.g., floods and droughts, in various parts throughout the world. Many scientific approaches for understanding these phenomena have been providing us a chance to prepare for the disastrous hazards such as torrential rainstorm, floods, and droughts.

Walker (1923), Walker and Bliss (1932) were the first to study the impacts of the Southern Oscillation (SO) on the Indian precipitation variability. Since then, a number of global scale studies related to the ENSO extreme phases showed various notable climatic links between precipitation patterns and either phase of these opposite extreme events in many areas throughout the globe. Since Berlage (1966) found the

Abbreviations: AI, Artificial Intelligence; CDF, Cumulative Density Function; DJF, December-February; ENSO, El Niño/Southern Oscillation; GMM, Gaussian Mixture Model; GEV, Generalized Extreme Value; ITS, Index Time Series; JJA, June-August; MAM, March-May; MI, Middle-Inland; NCEI, National Center for Environmental Information; NOAA, National Oceanic and Atmospheric Administration; NE, North-East; NW, North-West; PNA, Pacific North American; SLP, Sea Level Pressure; SON, September-November; SE, South-East; SO, Southern Oscillation; SOI, Southern Oscillation Index; SW, South-West; SPI, Standard Precipitation Index.

* Corresponding author.
E-mail address: june.lee@colostate.edu (J. Hong Lee).

https://doi.org/10.1016/j.jhydrol.2023.129206
Received 14 September 2022; Received in revised form 29 January 2023; Accepted 31 January 2023
Available online 4 February 2023

ENSO extreme events correlated well with precipitation anomalies on a global basis, Rasmusson and Carpenter (1983) related the precipitation and temperature patterns to the extreme phase of the Southern Oscillation and identified a significant link between the two variations. Also, Ropelewski and Halpert (1987, 1989) investigated temporal and spatial ranges showing consistent responses of the precipitation patterns over a variety of areas throughout the world to the extreme phases of the ENSO episodes and showed significant correlations of the ENSO forcing and precipitation patterns, which were also identified by Kiladis and Diaz (1989). More recently, Westra et al. (2013) used a Mann-Kendall nonparametric test and a nonstationary generalized extreme value analysis to identify monotonic trends in annual maximum daily precipitation on a global basis and to test for a significant association with near-surface air temperature averaged globally.

On a regional basis, many studies found plausible evidence of the ENSO far-reaching effect on the low and mid latitude climate variabilities as documented by Douglas and Englehart (1981), Rasmusson and Wallace (1983), Ropelewski and Halpert (1986), Redmond and Koch (1991), and Kahya and Dracup (1994). For midlatitude regions, several studies noted the ENSO–related precipitation correlation. For the southeastern United States, Douglas and Englehart (1981) revealed that the extreme ENSO forcing modulated the increases of the winter precipitation. Ropelewski and Halpert (1986) studied the climatic links between the extreme southern oscillation and precipitation anomalies over North America and showed the ENSO-related precipitation signals. This finding was also confirmed by Kiladis and Diaz (1989). Grimm et al. (1998) documented the influence of the extreme phases of SO on precipitation variability over southern Brazil using monthly precipitation data over 250 stations. In Turkey, some coherent regions where precipitation anomaly is statistically correlated with the extreme phases of ENSO events were found by Karabörk and Kahya (2003). Korea-Japan precipitation patterns were investigated by Jin et al. (2005) in relation to the ENSO far-reaching effects. They used lead-lag correlation analysis for five categorized Southern Oscillation Index (SOI) and non-exceedance precipitation probability time series and showed evidence of the ENSO-precipitation correlation. In Sri Lanka, the Kelani River basin was examined by Chandimala and Zubair (2007) focusing on the precipitation probability related to the ENSO events and sea surface temperature using principal component and correlation analyses. A coupled general circulation model was employed by Power et al. (2006) for investigating the climatic responses of Australian precipitation patterns to the ENSO forcing. Also, Cai et al. (2011) examined the ENSO effects on the precipitation pattern over Australia in terms of extra-tropical and tropical teleconnections triggered by the equatorial Pacific sea surface temperature. Lee and Julien (2016) showed teleconnection of the extreme phases of ENSO forcing and midlatitude precipitation variability in the Korean peninsula, and Wang et al. (2020) investigated the role of ENSO events in climatic links between Chinese precipitation patterns and tropical cyclones.

Previous studies of the ENSO-related teleconnection have focused more on the warm phase of extreme events and the impacts of the cold phase of extreme events have less scientific attention since the latter is considered less distinct and causes less disastrous natural hazards than the former. There has been few discussion in the literature about the teleconnections with a focus on comparative analysis and interpretation between the warm and cold phases of ENSO forcing. This study fills this gap by examining two potentially ENSO driven precipitation anomalies, in terms of their degree of magnitude and the temporal phase shift of the far-reaching impacts. As described in the relevant literature, many previous studies concentrated on global or rather broad regional scale analyses. Despite the various studies of the ENSO-related climate teleconnection, little is known about the perspective of ENSO forcing on sub-regional precipitation variability. Recently, precipitation occurred in more localized and intensified events and the corresponding hydrologic extremes had a devastating effect on people's lives, property, and the natural environment. Therefore, delving into the underlying influences of the extreme phases of climatic variation on various scopes of precipitation patterns provides a constructive way to predict and prepare unexpected natural hazards. Thus, it is important to investigate systematically how the warm and cold phases of extreme ENSO events influence the sub-regional precipitation patterns over the United States. Recently, more comprehensive information about spatial and temporal variability of hydrometeorological parameters is being sought by potential users of the climate information as they are modulated by the extreme phases of ENSO forcing. Prior literature investigated the teleconnection between the extreme phases of Southern Oscillation and precipitation anomalies over the United States using the observational precipitation data from 1931 to 1980 (50 years) covering only 11 ENSO episodes (Ropelewski and Halpert, 1986). However, we recently experienced noticeably severe extreme ENSO episodes including strong El Niño events in 1982, 1997, 2015 and strong La Niña events in 1988, 1999, 2010, and so on. This study aims to provide updated climate information regarding the temporal phase, spatial extent, and intensity of ENSO-related precipitation signals at each of several locations over the proposed study area using updated long-term precipitation data (1895–2020) spanning up to 29 ENSO episodes. In addition, from the perspective of methodological approaches, the present study provided an improved clustering technique. The previous studies including Ropelewski and Halpert (1986, 1987) used a subjective zoning method for determining core regions based on visual inspection over the harmonic dial maps. This subjective graphical approach implies that the ENSO-related hydrometeorological variability may include some uncertainties caused by other factors. In the present study, to categorize more objectively the candidate and core regions associated with the extreme phases of the ENSO forcing, an AI (Artificial Intelligence) machine learning technique was employed for determining the ENSO-related precipitation signal areas.

The main purpose of this study is to investigate precipitation variabilities over the United States associated with two opposite phases of ENSO events (warm and cold phases) using composite and harmonic analyses. This study uses an improved description of temporal cycle and spatial outlook for the intensity, time shift, and areal boundary of the ENSO-precipitation correlation. Also, the present study compares the two types of teleconnections induced by El Niño and La Niña considering magnitude and trend of the significant responses, using annual cycle and cross-correlation analyses.

2. Data

The monthly precipitation time series used in this study are based on 344 climate divisions covering all climate regions over the contiguous United States. The source of the applied dataset is the National Center for Environmental Information (NCEI) which is a governmental organization under the National Oceanic and Atmospheric Administration (NOAA). NOAA monitors and operates the overall United States meteorology. As shown in Fig. 1, the monthly precipitation sums data range from 1895 to 2020 and cover all the ENSO episodes (29 El Niño and 22 La Niña). For classifying the candidate regions objectively, Köppen climate classification is used in harmonic analysis. The contiguous United States was categorized into five main climate groups by the Köppen climate classification, e.g., A (tropical), B (arid), C (temperate), D (continental), and E (polar), with each group being divided based on seasonal precipitation and temperature patterns. To identify a consistent far-reaching effect of ENSO events on precipitation anomalies over the United States, two sets of extreme ENSO episodes are selected considering a comprehensive scope of criteria defined by Ropelewski and Halpert (1987, 1989), Rasmusson and Carpenter (1983), and Kiladis and Diaz (1989). The ENSO years for the two phases of extreme events selected in the present analysis are listed in Table 1. The Southern Oscillation Index (SOI) is applied as an indicator of representing large-scale climate variation over the central-eastern Pacific Ocean (ENSO). This present analysis applied the SOI data calculated and recorded by

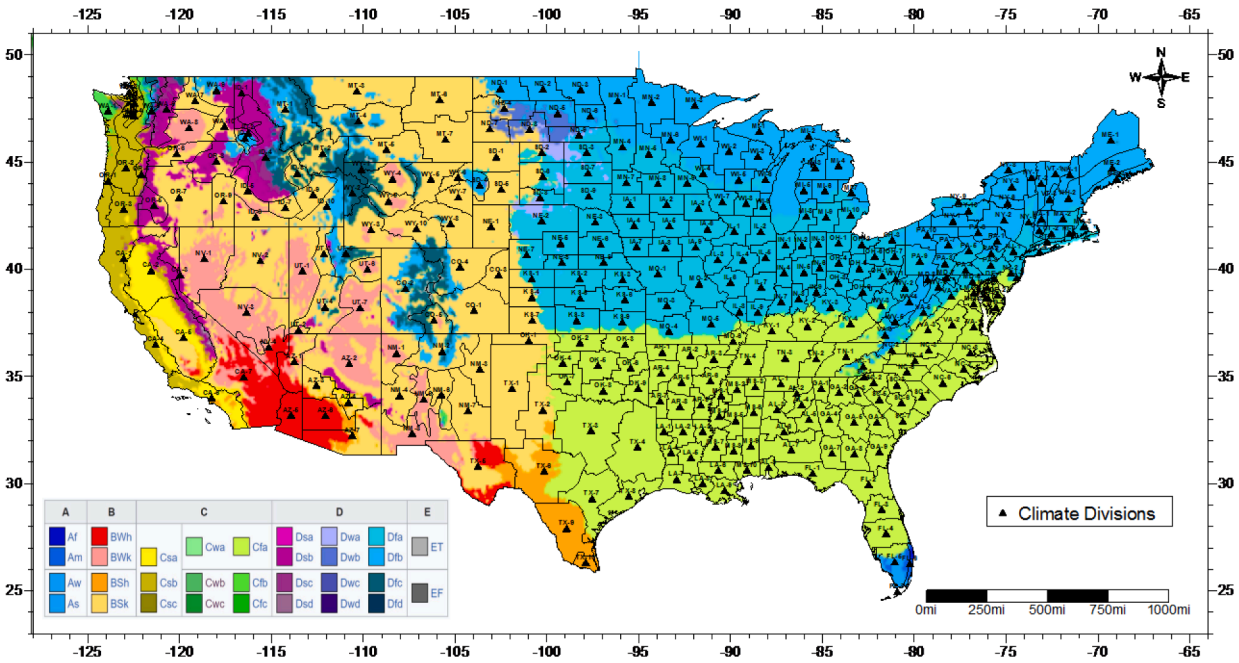

Fig. 1. Climate divisions and Köppen climate classification for precipitation indices.

Table 1
List of the ENSO episode years.

El Niño years	La Niña years
1905, 1911, 1914, 1918, 1923, 1925, 1930, 1932, 1939, 1941, 1951, 1953, 1957, 1963, 1965, 1969, 1972, 1976, 1982, 1986, 1991, 1994, 1997, 2002, 2004, 2006, 2009, 2015, 2018.	1910, 1915, 1917, 1924, 1928, 1938, 1950, 1955, 1964, 1971, 1973, 1975, 1985, 1988, 1995, 1998, 2000, 2005, 2007, 2010, 2011, 2017

the NOAA Climate Prediction Center. These SOI time series are computed based on the difference of the standardized sea level pressure (SLP) anomaly between Tahiti and Darwin, Australia.

3. Method

3.1. General concept

To examine the spatiotemporal extent to which El Niño/La Niña affect precipitation patterns over the United States, an empirical method

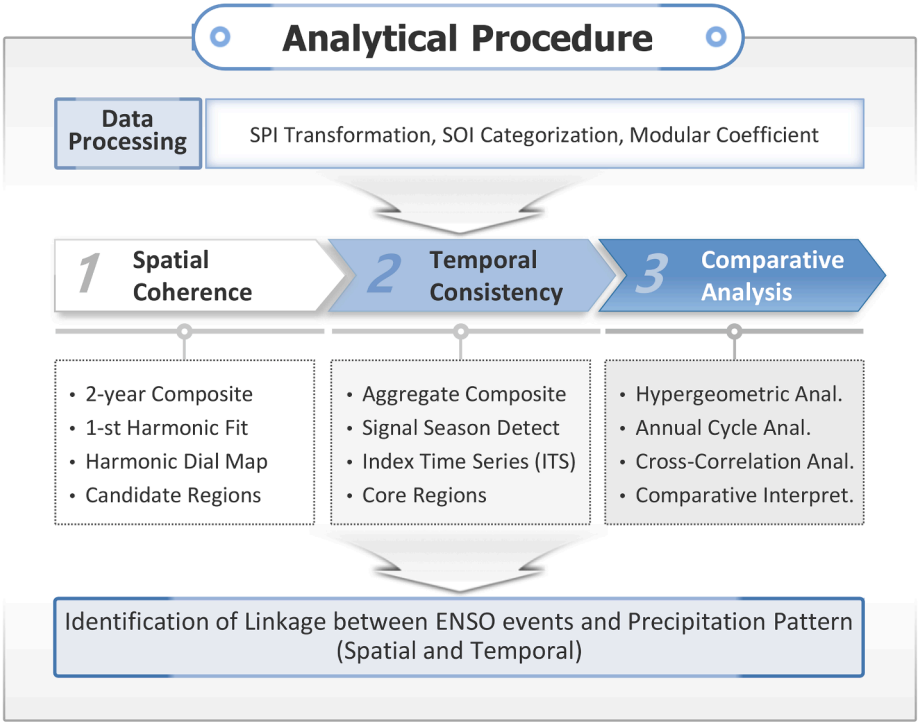

Fig. 2. Flowchart of the empirical methodology.

(Ropelewski and Halpert, 1986), annual cycle analysis, and cross correlation analysis are employed with some changes and additions. As shown in Fig. 2, the specific procedure of this analysis consists of mainly-three steps, namely, data processing, spatial and temporal analyses, and comparative statistical assessment. In the first step, the original raw data are transformed into appropriate data formats, e.g., ranked percentile, modular coefficients, and categorized SOIs. In the second step, candidate and core regions are determined using composite and harmonic analyses. Then, in the last step, El Niño/La Niña–related precipitation signals are compared using lag cross-correlation and annual cycle analyses.

3.2. Data processing

Monthly precipitation data of 344 climate divisions over the United States are fitted to a gamma distribution for calculating the Standard Precipitation Index (SPI) using a method developed by McKee et al. (1993). The SPI is a probability index that considers only precipitation for assessing drought and wet condition. As the dry and wet conditions become more severe, the index becomes more negative or positive. The

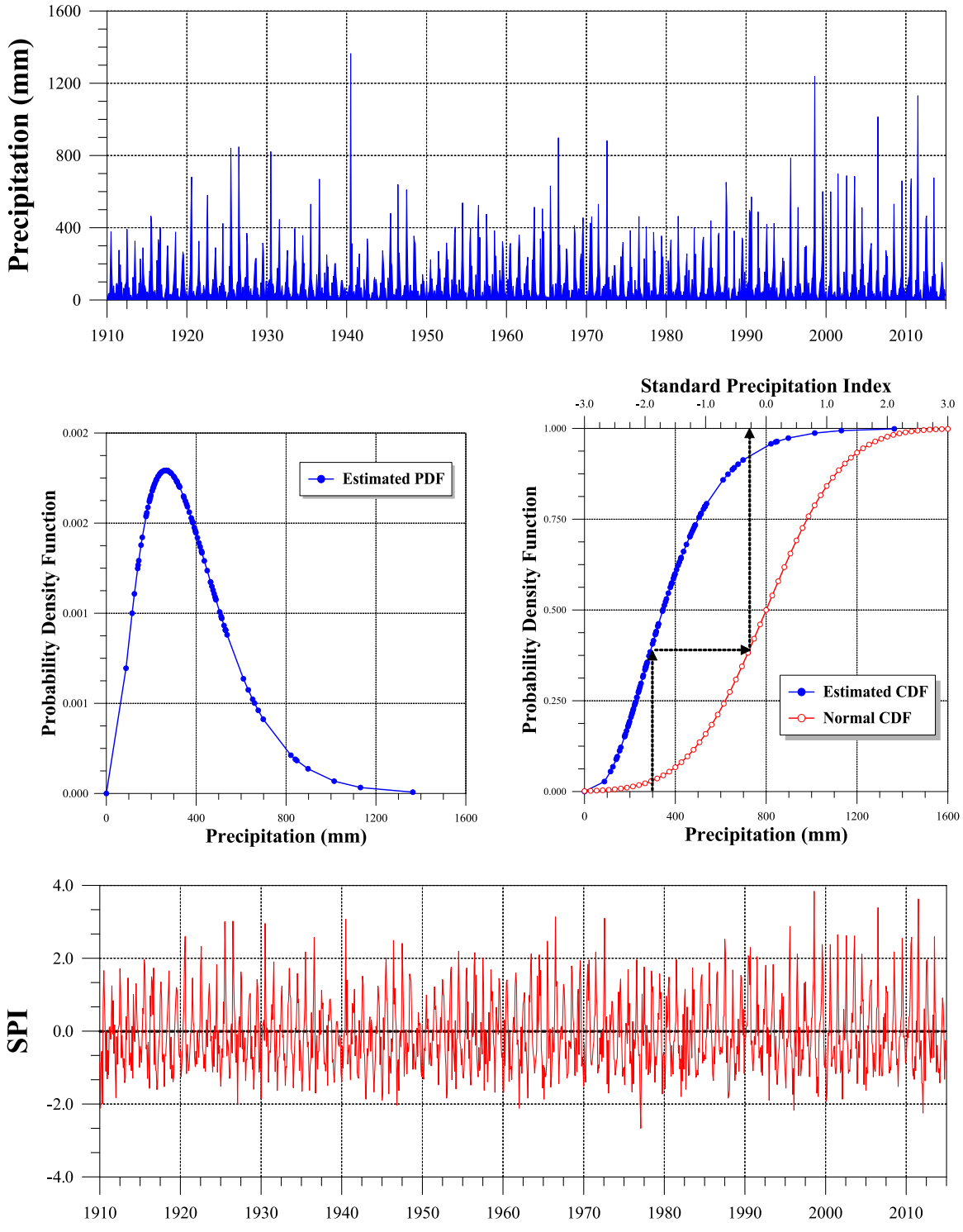

Fig. 3. SPI Estimation.

fitted distribution can be transformed into a cumulative density function (CDF) of the standard normal distribution by the equal-probability conversion technique as shown in Fig. 3. The SPI time series, which has a mean of zero and standard deviation of unity, is used in the composite and harmonic analyses. Monthly precipitation time series are transformed into modular coefficients for carrying out annual cycle analysis. These modular coefficients remove the effects of dispersed variance and mean values. The precipitation data are expressed as percentages for the annual mean values. The modular coefficient data are calculated by the rate of each monthly precipitation value to the monthly average value for the entire dataset. It places all divisions on the same cycle as the stationary condition of the cyclic feature of the values at the same time. In this present study, lag cross-correlation coefficients are computed from precipitation data and categorized SOI time series on a seasonal basis. To do this, four seasonal precipitation and SOI time series are formed by averaging three-month values. The four seasons consist of December-February (DJF), March-May (MAM), June-August (JJA), and September-November (SON). Then, all the SOI values are categorized into five levels based on the magnitudes of individual data (Jin et al., 2005). The five categories of the SOI values are strong warm phase, weak warm phase, normal phase, weak cold phase, and strong cold phase. On the other hand, the seasonal precipitation data are converted into percentile ranked probability time series to remove periodicities in precipitation time series and to deal with the disparities among climate divisions. The percentile ranked probability values are based on the Weibull plotting position formula. All precipitation values are ranked in ascending order and then divided by $n+1$ (n: size of data).

3.3. Spatial coherence

Monthly precipitation composites on a 24-month basis are computed for each climate division, starting with the July preceding the event, continuing through the June following the event year, for both high and low phases of the SO. The July preceding the event is designated as Jul (−), while the June following the event year is expressed as Jun (+). Composites are computed separately for each phase of the SO. The composite for each climate division is then fitted with the first harmonic of an idealized 24-month SO cycle (either warm or cold episodes). This method assumes one precipitation peak (or trough) during the duration of an SO event and that the SO is phase locked to the annual cycle. A 24-month compositing period was chosen since this defines the period during which one phase of the SO goes through its entire cycle (Rasmusson and Carpenter 1983). In the first harmonic cycle, the amplitude and phase of a harmonic dial refer to the strength and time of the response, respectively. That is, the amplitude refers to a representative magnitude of precipitation anomalies assumed to fluctuate in relation to the ENSO forcing and the phase indicates the timing of this fluctuation or the time at which the first harmonic has a maximum departure from the composite mean (Fig. 4). The formula of the harmonic fits are as follows (Wilks, 1995):

$$y_t = \bar{y} + \sum_{i=1}^{n/2}\left\{C_i\cos\left[\frac{2\pi it}{N} - \beta_i\right]\right\} = \bar{y} + \sum_{i=1}^{n/2}\left\{A_i\cos\left[\frac{2\pi it}{n}\right] + B_i\sin\left[\frac{2\pi it}{n}\right]\right\} \quad (1)$$

where,

$$A_i = \frac{2}{n}\sum_{t=1}^{n} y_t\cos\left(\frac{2\pi it}{n}\right), \quad B_i = \frac{2}{n}\sum_{t=1}^{n} y_t\sin\left(\frac{2\pi it}{n}\right), \quad C_i = \left(A_i^2 + B_i^2\right)^{0.5} \quad (2)$$

$$\beta_i = \tan^{-1}\frac{B_i}{A_i}\ (A_i > 0), \quad \frac{\pi}{2}\ (A_i = 0), \quad \tan^{-1}\frac{B_i}{A_i} \pm \pi\ (A_i < 0) \quad (3)$$

where y_t is monthly precipitation value, $\bar{y}$ is the mean precipitation value, t is time of observation, i is number of harmonic fits, n is sample size, C_i is amplitude of the harmonic curve (magnitude of curve), β_i is time of harmonic peak (temporal phase of curve), and A_i and B_i are Fourier coefficients.

After the climate division composites are fitted with a 24-month harmonic, the amplitude and phase of the curve is plotted as a vector for each station. In the analysis convention chosen here the vector points toward the positive part of the cycle, that is, wetter-than-normal precipitation. It is only after examining the composites, described below, that the actual sign of the SO-precipitation relationship can be

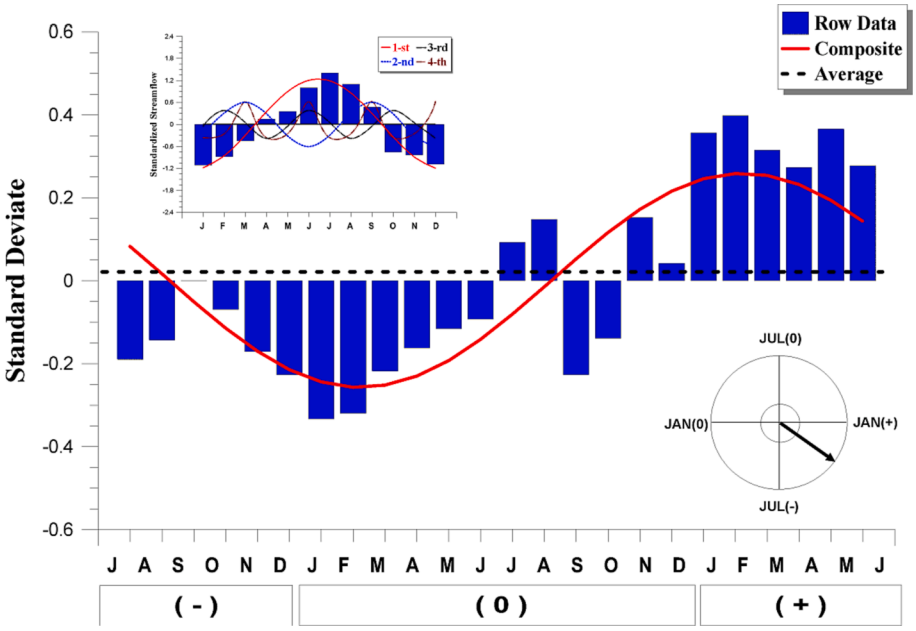

Fig. 4. A first harmonic fit to the precipitation ENSO composite for the climate division SC-5. The amplitude and the phase of the first harmonic are presented as a harmonic dial (the lower right). The inset diagram (the upper left) depicts an example illustrating several harmonic fits of annual cycle for monthly precipitation from the first to the fourth harmonic.

determined. This study is concerned with regional areas of the United States that exhibit strong SO-precipitation relationships over periods of many months. Therefore, individual, or isolated, climate division that shows strong apparent relationships or areas that have short-time scale relationships are not considered for further study.

The first harmonic for each point was replaced by a vector whose length and direction are equal to the amplitude and the phase of the harmonic, respectively. Plotting the harmonics as vectors, i.e., harmonic dial vectors, on a map provides a method to spatially identify candidate geographic areas that appear to have a coherent ENSO response. We attempted to choose the largest areas of coherent ENSO response, where the 'coherence (C)' is estimated through the computation of the ratio of the magnitude of the average vector to the arithmetic average value of the vector magnitudes. To determine regions of coherent harmonic vectors, the concept of 'coherence' is defined as

$$C = \frac{\left[\left(\sum V\cos\theta\right)^2 + \left(\sum V\sin\theta\right)^2\right]^{1/2}}{\sum V} \quad (4)$$

where C is coherence value, θ is angle of the vector, and V is magnitude of the vector. That is, the numerator is the average vector magnitude of all harmonic vectors within the candidate regions and the denominator is the arithmetic average value of the vector magnitudes.

The analysis that follows is limited to areas for which values of the coherence were equal to or greater than 0.80 (Ropelewski and Halpert, 1986). This eliminates from the analysis regions that contain harmonic vectors with large amplitudes at a few stations which have little consistency in phase, i.e., low coherence.

3.4. Temporal consistency

Aggregate composites are formed to detect the ENSO-related precipitation signal seasons. These signal seasons represent apparently consistent precipitation responses to extreme ENSO forcing. All ENSO composite values in a candidate region are averaged and plotted on a 24-month period to cover the entire ENSO cycle and identify accurately the signal season. One season within the aggregate composite is found by detecting a group of values showing more than five consecutive months with the same sign. The event year and the following year are regarded as the responding period of ENSO phenomena, considering the distance between the study area in midlatitude and the ENSO area in the Pacific Ocean. Index Time Series (ITS) are computed by temporally averaging precipitation values of the signal seasons for the entire years of record and by spatially averaging the precipitation data over the candidate regions. The ITS values are used to quantify the temporal consistency of the ENSO impact on precipitation patterns. Temporal consistency rates for the candidate regions are computed using the rate of the number of years exhibiting ENSO signals in ITS to the number of all ENSO event years. These temporal consistency rates are the determinant of the core regions showing consistent precipitation responses to ENSO phenomena. In addition, extreme precipitation events are examined in association with ENSO forcing as demonstrated by Ropelewski and Halpert (1986). They investigated climate linkage between ENSO events and extreme precipitation occurrences. In the present study, the number of years showing the ENSO-related extreme precipitation signal is counted during the signal season. To assign the highest and lowest levels of the extreme events, the ITS time series are ranked from the highest value to the lowest value, normalized by the entire dataset, and transformed to the probability time series (Kahya and Dracup, 1994). The highest value is assigned to the probability of 80% ITS, while the lowest value is assigned to the probability of 20% ITS.

A machine learning technique, Gaussian Mixture Model (GMM), was employed for diminishing the degree of subjectivity when candidate regions were determined based on the magnitude and temporal phase of the ENSO-related precipitation signals. The GMM algorithm is based on a statistical learning technique used in identifying a subset of discrete data which represents a feature space. As a measurable characteristic, the feature can describe phenomena being observed and the corresponding feature data can form a feature space by defining collectively the single or multidimensional range. For the purpose of classifying the candidate regions objectively, three features are selected in this study, i.e., the intensity of the ENSO-related precipitation teleconnection, temporal cycle of each precipitation response, and the Köppen climate classification. All harmonic dial vectors fall somewhere in the feature space. The GMM method takes advantage of a probability model instead of objective functions of distance measurements as opposed to the commonly used clustering techniques, e.g., fuzzy C-means or k-means, which are based on distance measures. In the GMM algorithm, each cluster is classified by a parametric probability density based on a mixture model of probability distribution followed by dataset, and the cluster structure is modeled by a finite mixture. Although the GMM technique has been considered a powerful tool for cluster analysis in many research fields, there has been little attention given to its practical application in hydro-climatological studies. The dimension of the input data affects the results of cluster analysis' largely because the GMM is based on a probability model. Therefore, it is of great importance to select an appropriate feature subset for conducting cluster analysis. Multivariate distributions of a given dataset can be fitted with a normal mixture model for clustering structure. The multivariate data, y_n, which are composed of m independent samples with variables, comprises C clusters in the dataset, and a probability distribution is assigned to each sample with a density function. A mixture probability density function, pdf, is weighed for the densities of C clusters as follows:

$$\mathrm{pdf}(y_n|\beta) = \sum_{i=1}^{C} p_i h_i(y_n|\mu_i, V_i) \quad (5)$$

where p_i is mixing proportions, h_i is normal probability density function, μ_i is mean of h_i, and V_i is variance matrix. If an indicator vector of y is $d = [d_1, \cdots, d_m]$ with $d_m = [d_{n1}, \cdots, d_{ni}]$, the mixture model log likelihood is as follows:

$$L(\beta|y_1, \cdots, y_m, d_{ni}) = \sum_{n=1}^{N} \ln\left[\sum_{i=1}^{C} d_{ni} p_i h_i(y_n|\mu_i, V_i)\right] \quad (6)$$

Also, the parameter $\beta = (p_1, \cdots, p_i, \mu_1, \cdots, \mu_i, V_1, \cdots, V_i)$ can be selected for maximizing the log-likelihood. Here, many normal mixture models can be chosen according to the geometric features of each cluster that includes the expression of the cluster variance matrix.

3.5. Comparative analyses

The hypergeometric distribution test is employed to assign the significance level of the ENSO-precipitation correlation. A cumulative probability computed from the hypergeometric distribution gives an occurrence significance level of the relationship previously defined for both extreme phases of the ENSO. Haan (1977) conducted the hypergeometric distribution test calculating "the cumulative probability that at least *m* successes are obtained in *n* trials from a finite population of size *N* containing *k* successes". Kahya and Dracup (1994) used the hypergeometric test in terms of average value and high-low extreme events. In the present test, two cases (I and II) are considered according to the definition of a success. In case I, a success is defined as the occurrence of years that an ITS value associated with ENSO events is higher (lower) than the median, while in case II, a success is defined as the occurrence of the year in which the values of an ITS are associated with ENSO events, falls in the upper (lower) 20% of the distribution. Annual cycle analysis is used as a comparative interpretation of two ENSO effects on the precipitation anomaly from the perspective of magnitude and annual trend of the signal. Monthly precipitation time series are transformed into modular coefficients for carrying out annual cycle analysis. These modular coefficients remove the effects of

dispersed variance and mean values. The precipitation data are expressed as percentages for the annual mean values. The modular coefficient data are calculated by the rate of each monthly precipitation value compared to the monthly average value for the entire data. These annual cycle plots make it possible to determine whether the extreme phases of warm and cold ENSO events modulate precipitation increasingly or decreasingly. Cross-correlation coefficients are calculated on a seasonal basis to compare the positive and negative ENSO-related precipitation signals. Five categorized SOI data sets like the ENSO index are correlated with the monthly precipitation time series expressed by percentile ranked probability. The resulting correlation coefficient values indicate the magnitude and sign of the relationship between the precipitation patterns and the ENSO forcing on a seasonal basis. More detailed explanation of the data conversion and correlation procedure was described in the data processing of the Method section.

4. Results

4.1. El Niño-precipitation relationship

Fig. 5 shows the harmonic dial map with the detected candidate regions from the results of composite and harmonic analyses. The vectorial map for precipitation indicates five regions of the United States that appear to have a coherent ENSO response. That is, the five candidate regions were detected, namely, the North-West region (NW), the South-West region (SW), the Middle Inland region (MI), the South-East region (SE), and the North-East region (NE). As shown in Table 2, composite precipitation indices for each region indicate that the NW, SW, MI, SW, and NE regions may have an ENSO-related response. The precipitation composites for the five candidate regions show clearly defined dry and wet seasons within the ENSO cycle and so they are explained in detail for further consideration in this analysis.

The North-West region (NW) includes 30 climate divisions, extending from Washington and northern Oregon to western Montana and northern Wyoming, and including almost all of Idaho. The South-West

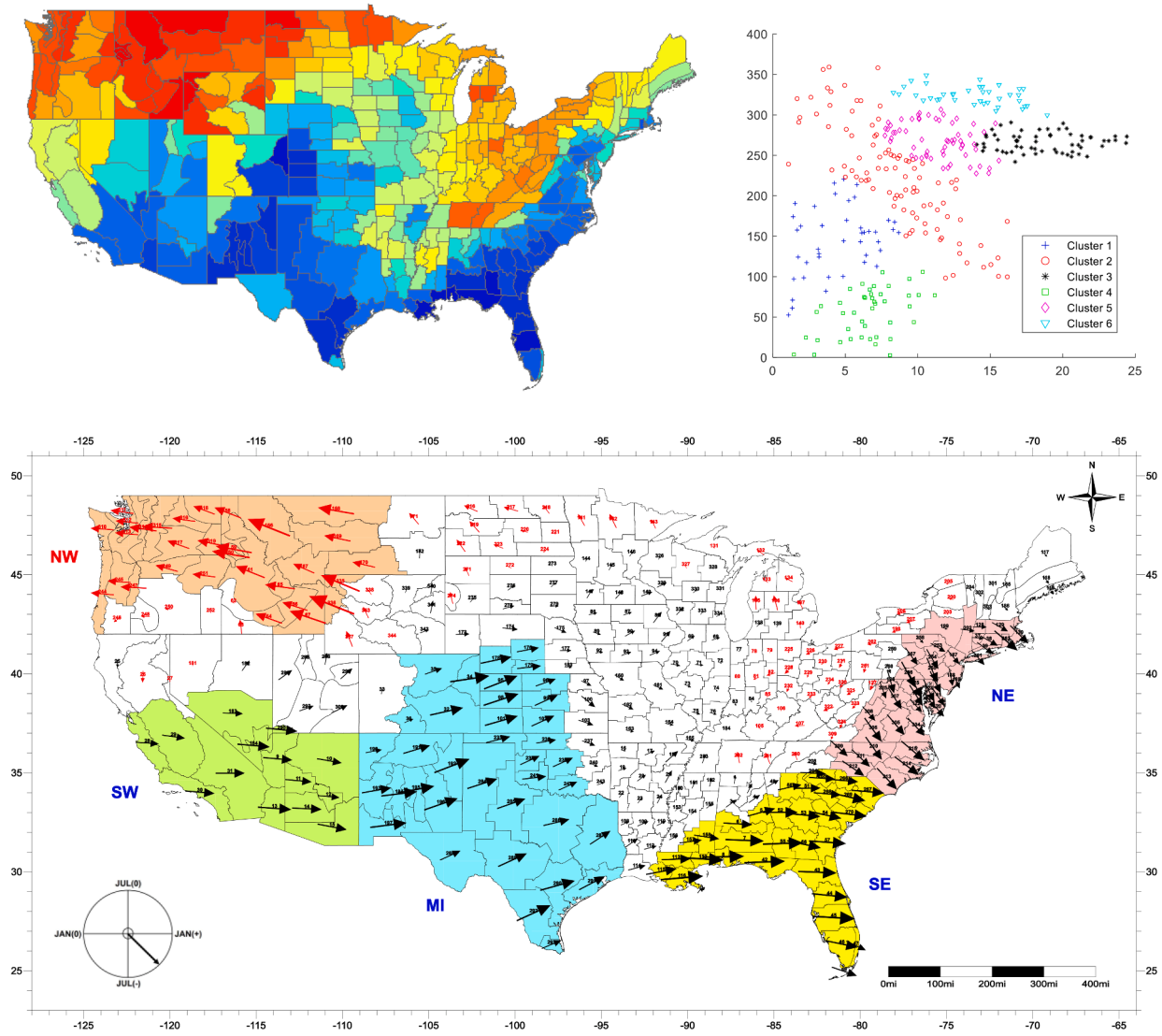

Fig. 5. Image map (upper left), clustering results (upper right) and harmonic dial map (lower) based on the first harmonic of the 2-year El Niño composites. Scale for the direction of arrows: south, July(−); west, January(0); north, July(0); and east, January(+). The magnitude of arrows is proportional with the amplitude of the harmonics. Five candidate regions were detected using vectorial mapping, namely, the North-West region (NW), the South-West region (SW), the Middle Inland region (MI), the South-East region (SE), and the North-East region (NE). The five colors were used for dividing the candidate regions based on the harmonic analysis results. The NW region showed below normal precipitation during the signal season of Nov (0) - May (+). The SW, MI, SE, and NE regions showed above normal precipitation during the signal seasons of Sep (0) - Apr (+), Oct (0) - Apr (+), Nov (0) - Mar (+), and Nov (0) - May (+), respectively.

Table 2
Properties of the candidate regions for El Niño events. Coherence values are to identify and quantify the candidate regions that appear to have a significant El Niño response which estimated using the ratio of the magnitude of the average vector to the arithmetic average value of the vector magnitudes. Total episodes stand for the number of El Niño events. Occurrence episodes are the number of years associated with the maximum positive sea surface temperature anomalies in the central-eastern Pacific. Consistency rates for the candidate regions are computed using the rate of the number of years exhibiting El Niño signal in ITS to the number of all El Niño event years which are the determinant of the core regions showing consistent precipitation responses to El Niño phenomena.

Region	Season	Coherence	Total Episode	Occurrence Episode	Consistency	Extreme Events
NW	Nov (0) – May (+)	0.96	29	22	76%	10
SW	Sep (0) – Apr (+)	0.99	29	24	83%	15
MI	Oct (0) – Apr (+)	0.99	29	25	86%	17
SE	Nov (0) – Mar (+)	0.98	29	24	83%	12
NE	Nov (0) – May (+)	0.99	29	21	72%	10

region (SW) occupies all of Arizona, the southern parts of California and Nevada, and part of Utah. The Middle-Inland region (MI) consists of eastern Colorado, western Kansas and Oklahoma, part of Nebraska, and all of New Mexico and Texas, and covers 37 climate divisions. The South-East region (SE) covers 32 climate divisions, and includes all of Florida and South Carolina, parts of Louisiana, Mississippi, Alabama, and almost all of Georgia. The North-East region (NE) has the smallest area but contains the largest number of climate divisions among all candidate regions. The NE region contains 42 climate divisions and covers almost all of North Carolina and Virginia, eastern Pennsylvania and New York, and Maryland, Delaware, New Jersey, Connecticut, Rhode Island.

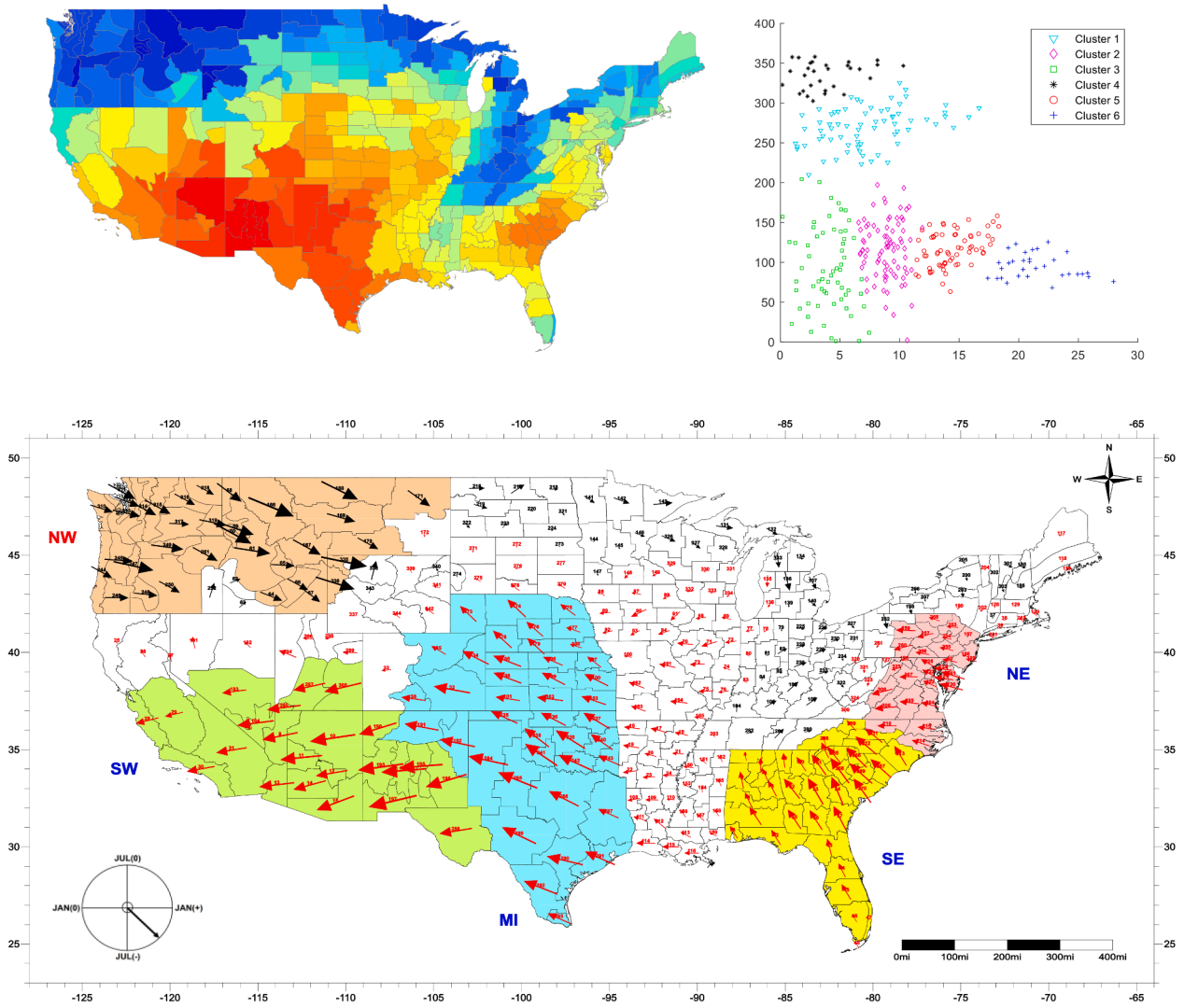

Fig. 6. Image map (upper left), clustering results (upper right) and harmonic dial map (lower) based on the first harmonic of the 2-year La Niña composites. Scale for the direction of arrows: south, July(−); west, January(0); north, July(0); and east, January(+). The magnitude of arrows is proportional with the amplitude of the harmonics. Five candidate regions were detected using vectorial mapping, namely, the North-West region (NW), the South-West region (SW), the Middle Inland region (MI), the South-East region (SE), and the North-East region (NE). The five colors were used for dividing the candidate regions based on the harmonic analysis results. The NW region showed above normal precipitation during the signal season of Oct (0) - Feb (+). The SW, MI, SE, and NE regions showed below normal precipitation during the signal seasons of Aug (0) - Jun (+), Oct (0) - Jun (+), Nov (0) - May (+), and Nov (0) - May (+), respectively.

4.2. La Niña-precipitation relationship

For 22 La Niña episodes, which are the cold phase of ENSO, the composite and harmonic analyses were performed on the monthly precipitation data. The resulting map of harmonic dial vectors (Fig. 6) indicates coherent responses within the five outlined regions, the North-West region (NW), the South-West region (SW), the Middle-Inland region (MI), South-East region (SE), and North-East region (NE). ENSO composites of precipitation indices for each of the regions indicate that the five regions have well-defined seasons of potentially significant ENSO-related response. The overall results of the composite and harmonic analyses are outlined in Table 3.

The North-West region (NW) occupies all of Washington, almost all of Oregon, Idaho, Montana, and the northwestern part of Wyoming, and covers 34 climate divisions. The South-West region (SW) includes 23 climate divisions, extending from southern California and to western Texas, and including all of Arizona, southern Nevada, and Utah, almost all of New Mexico. The Middle-Inland region (MI) covers 42 climate divisions, and includes all of Nebraska, Kansas, Oklahoma, eastern Colorado, northeastern New Mexico, and almost all of Texas. The South-East region (SE) consists of eastern North Carolina, and all of South Carolina, Georgia, Alabama, Florida, and covers 36 climate divisions. The North-East region (NE) has the smallest area, contains 29 climate divisions, and covers almost all of Virginia and Pennsylvania, part of North Carolina and West Virginia, and all of Maryland, Delaware, New Jersey.

4.3. Comparative analysis of El Niño and La Niña

The probability that the wet (dry) season occurs at random during the ENSO event years was tested by the hypergeometric distribution. In case I, the application of the hypergeometric distribution model results in a very low level of probability of occurrence by chance (less than 0.008) for both events. In case II, the probability is also very low for both phases of extreme events except for the SE region for the La Niña events. The extreme wet precipitation conditions appear to be almost exclusively related to ENSO events in the 125-yr period. Overall results in Tables 4 and 5 are also consistent with the high confirmation rates (72–86% for El Niño events and 77–82% for La Niña events) for temporal consistency of the signals. All of this implies that the relationship depicted in the aggregate composites is probably due to a nonrandom forcing mechanism, i.e., the tropical thermal anomalies. Monthly precipitation time series are transformed into modular coefficients for carrying out annual cycle analysis. From this resulting series, El Niño and La Niña composites are formed and plotted along with the regional annual cycle (Figs. 7 and 8). Examination of this figures reveals two fundamental features. First, for a typical precipitation behavior during El Niño events, a suppressed precipitation of the annual cycle during the event year is followed by an enhanced precipitation of the annual cycle from the end of event year to the beginning of the following year. Second, for typical precipitation behavior during La Niña events, a somewhat increased amplitude during the event year precedes a decreased amplitude from the end of the event year to the beginning of the following year. This enhancement and suppression of magnitudes are roughly concurrent with the previously detected wet and dry signal seasons in five core regions. Also, an opposite tendency in monthly precipitation fluctuations between the El Niño and the La Niña composites during a 24-month period are noticeable. In summary, the resulting findings suggest that the tropical heating (cooling) anomalies modulate the annual precipitation cycle within the United States by increasing (decreasing). Table 6 displays the results of calculating cross-correlation coefficients. These values represent the intensity and sign of the correlation between the ENSO phenomena and precipitation anomalies. This correlation analysis is conducted for the large-scale climate indicator (ENSO index) and the seasonal precipitation anomalies, which use five categorized SOI data sets and percentile ranked probabilities, respectively. As a result, the seasonal precipitation anomalies were significantly correlated with both extreme phases of SO at a 0.05 significance level. The highest positive correlation coefficient values are shown in the lag-0 to lag-2 cases over the NW region, and negative correlations are found in the lag-0 to lag-2 (lag-1 to lag-3) cases over the SW and MI (SE and NE) regions for the strong warm phase SOI condition. For the strong cold phase SOI condition, the highest negative correlation coefficient values are found at the NW region with lag-0 to lag-2 cases, and positive correlations are shown at the SW and MI (SE and NE) regions with lag-0 and lag-2 (lag-1 to lag-3) cases. As a result,

Table 4
Probabilistic assessments for significance level based on the hypergeometric distribution (El Niño events).

Case	Region	N	k	n	m	Probability
I	NW	125	63	29	22	0.002
	SW	125	65	29	24	0.001
	MI	125	66	29	25	0.001
	SE	125	62	29	24	0.000
	NE	125	59	29	21	0.002
II	NW	125	25	25	10	0.008
	SW	125	25	25	15	0.001
	MI	125	25	25	17	0.000
	SE	125	25	25	12	0.001
	NE	125	25	25	10	0.008

Table 5
Probabilistic assessments for significance level based on the hypergeometric distribution (La Niña events).

Case	Region	N	k	n	m	Probability
I	NW	125	65	22	17	0.008
	SW	125	63	22	18	0.001
	MI	125	67	22	18	0.003
	SE	125	61	22	17	0.003
	NE	125	66	22	17	0.010
II	NW	125	25	22	12	0.000
	SW	125	25	22	11	0.001
	MI	125	25	22	11	0.001
	SE	125	25	22	8	0.039
	NE	125	25	22	9	0.011

Table 3
Properties of the candidate regions for La Niña events. Coherence values are to identify and quantify the candidate regions that appear to have a significant La Niña response which estimated using the ratio of the magnitude of the average vector to the arithmetic average value of the vector magnitudes. Total episodes stand for the number of La Niña events. Occurrence episodes are the number of years associated with the maximum negative sea surface temperature anomalies in the central-eastern Pacific. Consistency rates for the candidate regions are computed using the rate of the number of years exhibiting La Niña signal in ITS to the number of all La Niña event years which are the determinant of the core regions showing consistent precipitation responses to La Niña phenomena.

Region	Season	Coherence	Total Episode	Occurrence Episode	Consistency	Extreme Events
NW	Oct (0) – Feb (+)	0.97	22	17	77%	12
SW	Aug (0) – Jun (+)	0.99	22	18	82%	11
MI	Oct (0) – Jun (+)	0.97	22	18	82%	11
SE	Nov (0) – May (+)	0.95	22	17	77%	8
NE	Nov (0) – May (+)	0.94	22	17	77%	9

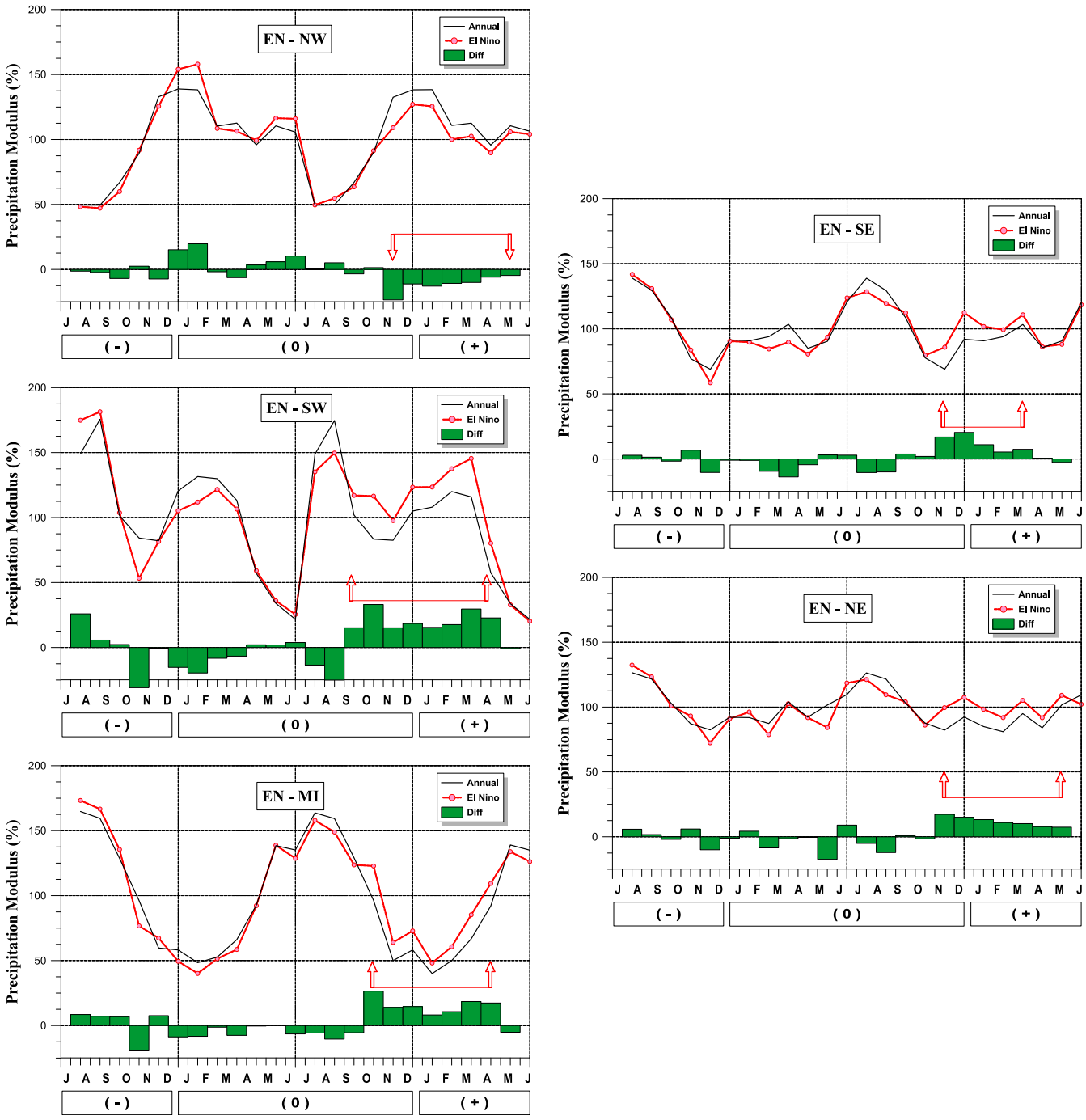

Fig. 7. The comparison between El Niño composite cycles (shown by dashed line) and annual cycles (shown by solid line) of the NW, SW, MI, SE, and NE regions, based on modular coefficients. Arrows indicate the beginning and end months of the ENSO signal season.

the stronger warm and cold phases of ENSO forcing, the more and less precipitation with lag time 0 to 3 seasons over the United States.

5. Discussion

As shown in Fig. 5, the results of this study show negative (positive) precipitation response to the El Niño events at the NW region (SW, MI, SE, and NE regions) during fall (0) to spring (+) seasons. Especially, the amplitude of the positive precipitation departure of an El Niño year in the MI and SE regions are even higher than that of non-El Niño years. On the contrary, during the cold phase of ENSO phenomena, the opposite patterns are detected. The monthly precipitation indices are wetter (drier) than normal for the NW (SW, MI, SE, and NE) core region from fall (0) through spring (+) seasons. The amplitude of the negative precipitation departure of the La Niña year at the SW and MI regions are much higher than that of a non-event year.

The opposite pattern of precipitation anomalies over the western parts of the United States (between the NW region and the SW region) was documented in earlier studies (Cayan and Webb, 1992; Emery and Hamilton, 1985; Cayan and Peterson, 1989) and it was consistently shown in the relevant composites of the extreme phase of ENSO forcing. Cayan and Webb (1992) stated that during the mature warm phase of the ENSO phenomena in association with deepening of the Aleutian Island low pressure the northward shift of the North Pacific storm paths'

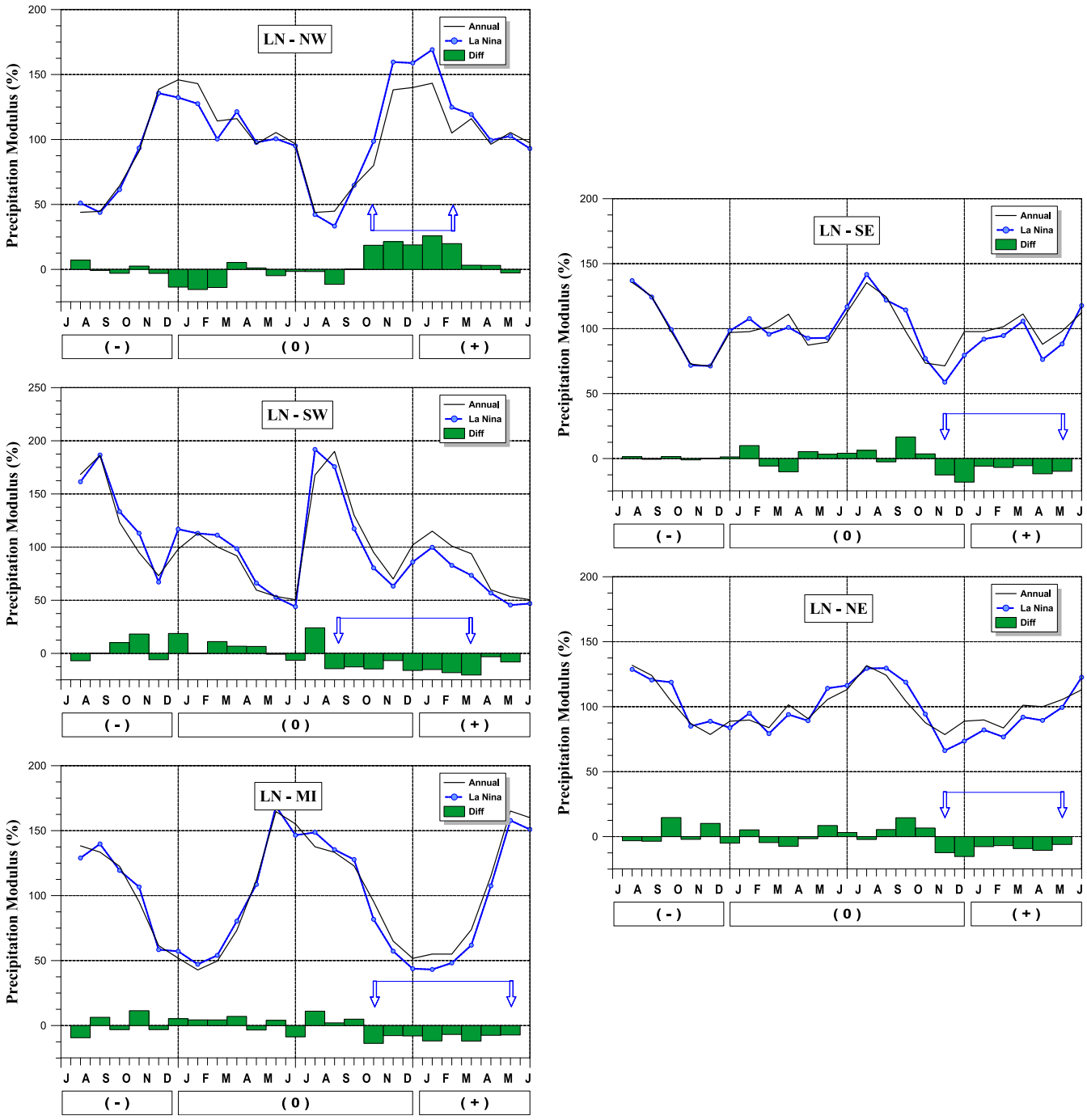

Fig. 8. The comparison between La Niña composite cycles (shown by dashed line) and annual cycles (shown by solid line) of the NW, SW, MI, SE, and NE regions, based on modular coefficients. Arrows indicate the beginning and end months of the ENSO signal season.

causes wet conditions over Alaska and western Canada and dry conditions over the northwestern US. On the other hand, the study by Emery and Hamilton (1985) showed that during the La Niña events the depression of the Central Pacific low, which is located over the Aleutian and Gulf of Alaska, modulates a more active low in the eastern Gulf of Alaska. These La Niña-related atmospheric activities affect the North Pacific winter storms shifting toward the northwestern United States. As a result, wetter-than-average precipitation patterns are observed over the NW region (Cayan and Peterson, 1989).

Douglas and Englehart (1984) investigated the US precipitation patterns in relation to the 1982–1983 ENSO event and linked the observed wet condition with intensification of a mid-latitude trough in the southwestern region of the United States. For the climatological causes for the teleconnection, Cayan and Webb (1992) revealed that the SW wet conditions during the ENSO years are attributed to the mid-latitude storm displacement by active southerlies bringing up moisture-laden air currents from the subtropical Pacific. Additionally, they showed drier-than-normal conditions during the La Niña events over the SW region. Webb and Betancourt (1990) noted that the development of the Aleutian low gives rise to the intensification of the SW frontal storms at the time of the extreme phase of ENSO. A study by Ely et al. (1992) using sea level geopotential height anomalies associated with hydrologic variation over the SW region indicated that the dominant storm-producing atmospheric circulation pattern is an anticyclone

Table 6
Cross-correlation coefficients with respect to regions.

Core Region		Strong El Niño SOI					Normal Condition					Strong La Niña SOI				
		lag-0	lag-1	lag-2	lag-3	lag-4	lag-0	lag-1	lag-2	lag-3	lag-4	lag-0	lag-1	lag-2	lag-3	lag-4
El Niño	NW	**0.72**	**0.61**	**0.63**	0.17	0.19	0.02	0.04	0.06	0.02	−0.05	**−0.35**	**−0.38**	**−0.31**	−0.03	−0.15
	SW	**−0.49**	**−0.67**	**−0.76**	0.00	−0.26	−0.17	−0.11	−0.08	−0.08	0.00	**0.33**	**0.39**	**0.37**	0.19	0.01
	MI	**−0.63**	**−0.52**	**−0.38**	−0.21	−0.04	−0.15	−0.12	−0.07	−0.02	0.07	**0.31**	**0.32**	**0.35**	**0.36**	0.21
	SE	−0.21	**−0.68**	**−0.69**	**−0.49**	−0.18	−0.07	−0.10	0.00	−0.02	−0.02	0.14	**0.43**	0.24	**0.53**	−0.11
	NE	−0.08	**−0.92**	**−0.82**	**−0.55**	−0.17	−0.02	−0.05	0.00	−0.02	−0.05	−0.12	**0.32**	**0.31**	**0.55**	0.17
La Niña	NW	**0.68**	**0.56**	**0.53**	0.12	0.16	0.02	0.05	0.05	0.02	−0.04	**−0.37**	**−0.39**	**−0.32**	−0.04	−0.16
	SW	**−0.46**	**−0.64**	**−0.53**	0.09	0.12	−0.17	−0.11	−0.08	−0.06	0.04	**0.34**	**0.42**	**0.39**	0.28	0.13
	MI	**−0.47**	**−0.50**	**−0.37**	−0.10	0.13	−0.09	−0.10	−0.06	−0.03	0.00	**0.32**	**0.33**	**0.37**	**0.42**	0.05
	SE	−0.19	**−0.58**	**−0.68**	**−0.47**	−0.14	−0.05	−0.08	0.01	−0.01	−0.02	0.05	**0.51**	0.29	**0.64**	0.05
	NE	−0.20	**−0.84**	**−0.77**	**−0.50**	−0.21	0.02	−0.04	0.02	−0.01	−0.06	0.14	**0.37**	**0.35**	**0.75**	0.19

over the Gulf of Alaska and a cyclone off the California coast. Andrade and Sellers (1987) examined significant changes in tropical cyclogenesis during ENSO episodes considering a possible influence of the presence of warm sea surface temperature off the coast of California and pointed out that these atmospheric changes cause frequent tropical cyclone dissipating over Arizona. Also, they emphasized that during the warm ENSO phase anomalous warm water of the west coast of the SW region is a driver of the enhanced precipitation pattern in fall and spring seasons, which is the source of energy for the strengthened troughs. This warm water weakens the trade wind inversion caused by sinking air resulting from subtropical high. As a result, the warm water allows more moisture-bearing air to enter over the SW region. From the perspective of storage effects, the findings of Andrade and Sellers (1988) are consistent with the results of the present study in that the positive ENSO-related precipitation signal has been detected in fall to spring seasons. The SW region is one of regions over the United States in which cloudiness correlates significantly with the sea surface temperature over the tropical Pacific Ocean. Angell and Korshover (1987) employed a combined parameter of sunshine duration and cloud amount as a cloudiness index and identified a significant increase of cloudiness over the SW during 1950 to 1985. They showed that during the warm phase of ENSO forcing cloudiness is 5% above average, while below normal cloudiness exhibits at the time of cold events. In addition, Douglas and Englehart (1981) showed a significant correlation between tropical rainfall index and precipitation pattern of the SW region and emphasized that the teleconnection could be explained by the eastward moving low latitude troughs and the corresponding cloudiness. Webb and Betancourt (1990) analyzed simultaneous and lag relationships between precipitation in the Line Islands and Tucson, Arizona, and pointed out tropical cloud masses moving northeastward from the central tropical Pacific as a driving factor of the significant correlation. This implies that the subtropical jet stream enhanced by the equatorial convection produces more intense storm systems over the SW region.

An explanation for the apparent ENSO-related signal in the MI region is difficult to construct. To find the physical mechanisms for the increased (decreased) precipitation in the signal seasons, and the persistence of this apparent signal, Douglas and Englehart (1984) investigated the heavy precipitation over the United States associated with 1982–1983 ENSO event and indicated that enhanced precipitation could be linked with the development of a midlatitude trough over the southern part of the country. Although positive sea surface temperature anomalies are not a normal ENSO-related feature in the northeastern Pacific in the ENSO cycle (Norton et al., 1985), the occurrence of warm water might help to increase precipitation amounts in the MI region. The precipitation response in the southeastern United States to the ENSO phenomena is consistent with Ropelewski and Halpert (1986), Douglas and Englehart (1981). Ropelewski and Halpert (1986) stated that the precipitation response to ENSO may be more easily explained in terms of direct or shorter-range effects related to the enhanced subtropical jet stream and warmer than normal surface water over the Pacific. Douglas and Englehart (1981) suggested that the ENSO-related precipitation signal may be an indication of a more direct link to ENSO forcing than a Pacific North American teleconnection pattern (PNA). Active ENSO-related convection is typical in the equatorial Pacific, south of the southeastern United States. This convection has been linked to stronger than normal westerlies in the southern parts of the United States including Gulf of Mexico (e.g., 200 mb ENSO composites in Arkin, 1982) and hence a tendency for more frequent storms and precipitation in the southeastern United States. This possible direct link to the ENSO-related forcing may account for the consistent precipitation response over the southeastern US. Rasmusson and Wallace (1983) found a strengthened subtropical jet stream displaced southward from its normal position during the mature phases of ENSO event (1982–1983). This pronounced intensification of the jet stream drove numerous winter storms causing flooding events in the southern parts of the United States. Additionally, they indicated that this region has shown abnormal wet conditions associated with past ENSO events. Tropical cyclones infiltrating into the region increase and decrease precipitation but are not the only mechanism responsible for the positive and negative precipitation responses during the warm and cold phases of ENSO forcing. Simonson et al. (2022) stated that the occurrence of these precipitation patterns could be connected with southward shifted storm tracks over the NE region. The circulation shifts are associated with intensified precipitation because of southerly wind anomalies and modulate enhanced moisture-laden air transport into the region. During the ENSO event years, the persistent occurrence of warm/cold sea surface temperatures over the central and eastern equatorial Pacific triggers large-scale atmospheric fluctuations in the middle latitude based on complex air-sea coupled interactions. As a result, these ENSO-related middle latitude circulations excite abnormal precipitation patterns over the United States.

6. Summary and conclusions

Teleconnection between two phases of ENSO thermal forcing and monthly precipitation anomalies in the United States was investigated using a set of empirical and statistical analyses, such as harmonic analysis, annual cycle composites, and cross-correlation analysis. The details of the general results for ENSO-related precipitation signals are outlined in Tables 2 to 5. From the results of vectorial mapping through composite and harmonic analyses, the proposed study area is classified into five core regions designated as the North-West region (NW), the South-West region (SW), the Middle-Inland region (MI), the South-East region (SE), and the North-East region (NE). They showed high levels of spatial coherence and temporal consistency with notable spatial range and amplitude of the precipitation response to ENSO phenomena. The main conclusions are outlined as follows.

During the El Niño events, the monthly precipitation anomalies are below normal in the NW region, and above normal in the SW, MI, SE, and NE regions. For the NW region, the Nov (0) to Mar (+) is the signal seasons showing the noticeable consistency in precipitation in association with the warm ENSO forcing, and the Sep (0) to Apr (+), Oct (0) to Apr (+), Nov (0) to Mar (+), and Nov (0) to Mar (+) are the signal

seasons having a high level of temporal consistency in ENSO-related precipitation responses for the SW, MI, SE, and NE regions, respectively. The spatial coherence of the five core regions for the warm thermal forcing ranges from 0.96 to 0.99 and the temporal consistency are between 0.72 and 0.86. Especially, the MI core region showed the highest magnitude of the positive precipitation departure for the El Niño years. For the La Niña events, the monthly precipitation anomalies are above normal in NW region, and below normal in the SW, MI, SE, and NE regions. The results of the composite and harmonic analyses show that the signal season for wet period is October (0) to February (+), and the signal seasons for dry periods are Aug (0) to Jun (+), Oct (0) to Jun (+), Nov (0) to May (+), and Nov (0) to May (+) for the SW, MI, SE, and NE regions, respectively. The spatial coherence rates for the five core regions for La Niña events range from 0.94 to 99, and the temporal consistency for each core region are 0.77 to 0.82. Comparative analyses of precipitation responses to both warm and cold ENSO events reveal the high significance level of the ENSO-precipitation correlation with an opposite tendency in monthly precipitation anomalies. The NW region shows negative (positive) tendency for warm (cold) phases, while the SW, MI, SE, and NE regions show positive (negative) responses to the warm (cold) phases of ENSO episodes.

Above normal precipitation anomalies during the El Niño thermal forcing are more significant than below normal precipitation departures during the La Niña events. From the results of annual cycle analysis, the tropical heating and cooling anomalies of sea surface temperature modulate the annual precipitation cycle over the United States by increasing or decreasing. The highest positive (negative) correlation coefficient values are shown in the lag-0 to lag-2 cases for the NW core regions for the strong warm (cold) phase SOI condition. For the SW and MI regions, negative (positive) correlations are found in lag-0 to lag-2 cases for strong warm (cold) phase SOI condition and the same correlations are shown in lag-1 to lag-3 cases for the SE and NE regions. That is, the stronger warm and cold phases of ENSO forcing, the more and less precipitation with lag time 0 to 3 seasons over the United States. From the findings above, it is concluded that middle latitude precipitation responses to the El Niño and La Niña phenomena are detectable over the contiguous United States.

CRediT authorship contribution statement

Jai Hong Lee: Conceptualization, Methodology, Software, Writing – original draft, Investigation, Supervision. **Pierre Y. Julien:** Conceptualization, Validation. **Seungho Lee:** Data curation, Visualization.

Declaration of Competing Interest

The authors declare that they have no known competing financial interests or personal relationships that could have appeared to influence the work reported in this paper.

Data availability

Data will be made available on request.

References

Andrade, E.R., Sellers, W.D., 1987. El Niño and its effect on precipitation in Arizona. J. Clim. 8, 403–410.

Angell, J.K., Korshover, J., 1987. Variability in United States cloudiness and its relation to El Niño. J. Climate Appl. Meteor. 26, 580–584.

Arkin, P.A., 1982. The relationship between interannual variability in the 200 mb tropical wind field and the Southern Oscillation. Mon. Wea. Rev. 110, 1393–1404.

Berlage, H.P., 1966. The Southern Oscillation and world weather. Meteor. Inst. Meded. Verh. 88, 152 pp.

Cai, W., Rensch, P.V., Cowan, T., 2011. Teleconnection pathways of ENSO and the IOD and the mechanisms for impacts on Australian rainfall. J. Clim. 24, 3910–3923.

Cayan, D.R., Peterson, D.H., 1989. The influence of North Pacific atmospheric circulation on streamflow in the West, in Aspects of climate variability in the Pacific and the Western Americas, Amer. Geophys. Union, Monogr. 55, 375–397.

Cayan, D.R., Webb, R.H., 1992. In: El Niño/Southern Oscillation and Streamflow in the Western United States, in El Niño: Historical and Paleoclimatic Aspects of the Southern Oscillation. Cambridge University Press, pp. 29–68.

Chandimala, J., Zubair, L., 2007. Predictability of streamflow and rainfall based on ENSO for water resources management in Sri Lanka. J. Hydrol. 335, 303–312.

Douglas, A.E., Englehart, P.J., 1981. On a statistical relationship between autumn rainfall in the central equatorial pacific and subsequent winter precipitation in Florida. Mon. Weather Rev. 109, 2377–2382.

Douglas, A.E., Englehart, P.J., 1984. Factors leading to the heavy precipitation regimes of 1982–1983 in the United States. Proc. Of the Eighth Annual Climate Diagnostics Workshop. Washington, DC, pp. 42–54.

Ely, L. L., Enzel, Y., Cayan, D. R., 1992. Anomalous atmospheric circulation and large winter floods in six subregions of the southwestern United States, Proc. Of the Eighth Annual Pacific Climate (PACLIM) Workshop, 179-186.

Emery, W.J., Hamilton, K., 1985. Atmospheric forcing of interannual variability in the northeast Pacific Ocean: Connections with El Niño. J. Geophys. Res. 90, 857–868.

Grimm, A.M., Ferraz, S.E.T., Gomez, J., 1998. precipitation anomalies in Southern Brazil associated with El Niño and La Niña Events. J. Clim. 11, 2863–2880.

Haan, C.T., 1977. Statistical Methods in Hydrology. Iowa State University Press, Ames, IA.

Jin, Y.H., Kawamura, A., Jinno, K., Berndtsson, R., 2005. Quantitative relationship between SOI and observed precipitation in southern Korea and Japan by nonparametric approaches. J. Hydrol. 301, 54–65.

Kahya, E., Dracup, J.A., 1994. The influences of Type 1 El Niño and La Niña events on streamflows in the Pacific southwest of the United States. J. Clim. 7, 965–976.

Karabörk, M.Ç., Kahya, E., 2003. The teleconnections between extreme phases of Southern Oscillation and precipitation patterns over Turkey. Int. J. Climatol. 23, 1607–1625.

Kiladis, G.N., Diaz, H.F., 1989. Global climatic anomalies associated with extremes in the Southern Oscillation. J. Clim. 2, 1069–1090.

Lee, J.H., Julien, P.Y., 2016. Teleconnections of the ENSO and South Korean precipitation patterns. J. Hydrol. 534, 237–250.

McKee, T.B., Doesken, N.J., Kleist, J., 1993. The relationship of drought frequency and duration to time series. In: 8th Conference on Applied Climatology, pp. 179–187.

Norton, J., Mclain, D., Brainard, R., Husby, D., 1985. The 1982–83 El Niño event off Baja and Alta California and its ocean climate context. University of Washington Press, Seattle, pp. 44–72.

Power, S.B., Haylock, M., Colman, R., Wang, X., 2006. The predictability of Interdecadal changes in ENSO activity and ENSO teleconnection. J. Clim. 19, 4755–4771.

Rasmusson, E.M., Carpenter, T.H., 1983. The relationship between eastern equatorial Pacific sea surface temperatures and rainfall over India and Sri Lanka. Mon. Wea. Rev. 111, 517–528.

Rasmusson, E.M., Wallace, J.M., 1983. Meteorological aspects of the El Niño/southern oscillation. Science 222, 1195–1202.

Redmond, K.T., Koch, R.W., 1991. Surface climate and streamflow variability in the western United States and their relationship to large circulation indices. Water Resour. Res. 27 (9), 2381–2399.

Ropelewski, C.F., Halpert, M.S., 1986. North American precipitation and temperature patterns associated with El-Niño-Southern oscillation (ENSO). Mon. Weather Review 114, 2165–2352.

Ropelewski, C.F., Halpert, M.S., 1987. Global and regional scale precipitation patterns associated with the El Niño/Southern Oscillation. Mon. Wea. Rev. 115, 1606–1626.

Ropelewski, C.F., Halpert, M.S., 1989. Precipitation patterns associated with the high index phase of the southern oscillation. J. Clim. 2, 268–284.

Simonson, J.M., Birkel, S.D., Maasch, K.A., Mayewski, P.A., Lyon, B., Carleton, A.M., 2022. Association between recent U.S. northeast precipitation trends and Greenland blocking. Int. J. Climatol. 42 (11), 5682–5693.

Walker, G.T., 1923. Correlation in seasonal variations of weather, V III, A preliminary study of world weather. Mem. Indian Meteorol. Dep. 24, 75–131.

Walker, G.T., Bliss, E.W., 1932. World Weather V. Mem. Roy. Meteor. Soc. 4 (36), 53–84.

Wang, L., Yang, Z., Gu, X., Li, J., 2020. Linkages between tropical cyclones and extreme precipitation over China and the role of ENSO. Internat. J. Disaster Risk Sci. 11, 538–553.

Webb, R.H., Betancourt, J.L., 1990. Climatic effects on flood frequency: An example from southern Arizona. In: Proceeding of the Sixth Annual Pacific Climate (PACLIM) Workshop, Report. California State Dept. of Water Resources, Sacramento, pp. 61–66.

Westra, S., Alexander, L.V., Zwiers, F.W., 2013. Global increasing trends in annual maximum daily precipitation. J. Clim. 26, 3904–3918.

Wilks, D.S., 1995. Statistical Methods in Atmospheric Sciences. Academic Press, pp. 330–334.

WMO, 2014. El Niño/Southern Oscillation. WMO-No. 1145, 2–4.